A particle-based image segmentation method for phase separation and interface detection in PIV images of immiscible multiphase flow

Yaofa Li, Gianluca Blois, Farzan Kazemifar, Kenneth T Christensen

Li, Y., Blois, G., Kazemifar, F., & Christensen, K. T. (2021). A particle-based image segmentation method for phase separation and interface detection in PIV images of immiscible multiphase flow. Measurement Science and Technology, 32(9), 095208.

https://doi.org/10.1088/1361-6501/abf0dc

A Particle-Based Image Segmentation Method for Phase Separation and Interface Detection in PIV Images of Immiscible Multiphase Flow

Yaofa Li[1], Gianluca Blois[2], Farzan Kazemifar[3] and Kenneth T. Christensen[2,4,5]

[1]Department of Mechanical & Industrial Engineering Montana State University, Bozeman, MT 59717, USA

[2]Department of Aerospace and Mechanical Engineering, University of Notre Dame, Notre Dame, IN 46556, USA

[3]Department of Mechanical Engineering, San Jose State University, San Jose, CA 95192, USA

[4]Mechanical, Materials and Aerospace Engineering & Civil, Architectural and Environmental Engineering, Illinois Institute of Technology, Chicago, IL 60616, USA

[5]International Institute for Carbon-Neutral Energy Research (I2CNER), Kyushu University, Fukuoka, Japan

E-mail: `yaofa.li@montana.edu`

Received: December 2020

Abstract. Particle image velocimetry (PIV) is a valuable tool for experimentally studying multiphase flows. In order to distinguish the flow dynamics of each individual phase, proper image segmentation must be performed. In immiscible multiphase flows, the fidelity of phase segmentation is directly linked to the accuracy of the interface detection. This paper reports a novel method for robust phase separation and phase boundary identification applicable to particle images acquired via PIV. The method, which requires a seeding density differentiation between the phases, is based on particle detection and triangular meshing. In this method, tracer particles in all seeded phases are first identified, and the coordinates of the particle locations are then used to formulate a 2D unstructured mesh, where the triangular grids provide the basis for phase separation and the outer edges provide a basis for interface detection. This paper presents a parametric analysis on synthetic particle images to assess the performance of the method and to compare the results to existing approaches. In addition, an application to experimentally generated images is reported. These results show that this method can successfully track the complex interface evolution in a particularly challenging flow system consisting of immiscible multiphase flow in porous media.

Keywords: Particle detection, Phase discrimination, Particle image velocimetry, Multiphase flow, Porous media

Submitted to: *Meas. Sci. Technol.*

1. Introduction

Particle image velocimetry (PIV) is a powerful tool in experimental fluid mechanics and is commonly applied in the study of multiphase flows [1, 2, 3, 4, among others]. A prerequisite to proper application of PIV in such systems is the ability to perform *phase discrimination* or *segmentation* through the identification of each phase boundary prior to image interrogation. If these image pre-processing steps are not carefully performed, the particle tracers in the vicinity of the phase boundaries could be assigned to the wrong phase, leading to measurement artifacts that are particularly severe near interfaces. As such, erroneous reconstructions of fluid–fluid interfaces could result in misleading interpretation, not only of its structure, but also of its dynamics. Additionally, unlike single-phase flows, where manually-defined static masks delineating fluid–solid interfaces are often sufficient, in a multiphase flow, boundaries typically move and deform with time. Dynamically evolving boundaries due to deformable surfaces and/or moving objects could also benefit from phase separation implemented in an automated manner, especially when large PIV datasets are available [3, 5].

Immiscible multiphase flows in porous media represent one of the most challenging flow systems to study with optical diagnostics [6]. These flows are central to a range of industrial and environmental processes, including enhanced oil recovery (EOR) [7], ground water remediation [8], water management in fuel cells [9] and carbon capture and storage (CCS) [10]. Numerical methods to study the pore-scale physics near the meniscus struggle due to the strong instabilities characterising phase discontinuities where capillary forces play a crucial role. Recent studies carried out via microscopic PIV (μPIV) have proven quite valuable for elucidating some of the physics associated with these instabilities, particularly in providing direct quantification of transient pore-scale events [11, 12, 13, 14, 15]. However, this work has also exposed technical challenges associated with pre-processing large high-speed image datasets with the intention of identifying complex phase boundaries. These boundaries are in fact formed by a constellation of disconnected regions of flow that have proved extremely difficult to detect via automatic methods.

Several techniques have been proposed to achieve phase separation in PIV images and can be classified in three general categories [3, 5]: (*i*) optical separation during the image acquisition stage (*i.e.*, color-based separation) (*ii*) digital separation prior to PIV analysis (*i.e.*, intensity discrimination, feature size discrimination, feature shape discrimination, spatial frequency discrimination, direct boundary detection, etc.) and (*iii*) correlation peak separation post PIV cross-correlation analysis. Each category of method has advantages and shortcomings. For instance, while color-based separation is known to yield almost perfect discrimination through the use of laser-induced fluorescence (LIF), it is also recognized that the fluorescent light obtained this way is weaker than directly scattered light which introduces optimization issues in the illumination. Moreover, when more than two fluid phases are present, multiple band windows are needed, which substantially increases the complexity and cost of the experimental setup. Although intensity-based discrimination, which relies on simple thresholding, is popular and easy to implement, its uncertainty can be as high as several pixels [16]. This method is also susceptible to uneven illumination, a very common issue in PIV measurement. Other methods are tailored to certain specific applications and cannot easily be implemented to a broad spectrum of cases. For instance, feature shape discrimination is only applicable when one of the phases

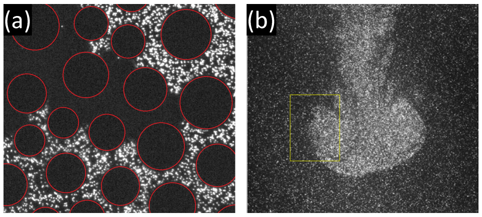

Figure 1. Examples of PIV images showing cases of multiphase flows in which image segmentation and interface detection is required: (a) immiscible multiphase flow of CO_2 (dark regions) and water (seeded regions) in a 2D micromodel featuring randomly distributed circular posts of heterogeneous size (red circles) [14]; (b) a turbulent vortex ring generated by the impulsive ejection of water that is densely seeded with particles through a nozzle into a quiescent environment that is more sparsely seeded [24].

exhibits a distinctive pattern [17]. Likewise, the correlation peak discrimination method is only applicable when there exists a significant velocity difference between different phases at a given location [18]. The reader is referred to refs. [4, 3, 16, 5] for more comprehensive reviews of existing methods. It is worth noting that, recently, image segmentation based on deep learning approaches applying convolutional neural networks (CNN) has been reported [19, 20]. However, while these approaches have achieved impressive results in a number of applications across several disciplines, each network architecture must be tailored for a specific image type and trained on extremely large ground-truth datasets. Currently, very few networks have been developed for fluid mechanics applications and, more importantly, to the best of our knowledge, experimentally-obtained training datasets are unavailable for multiphase flows. In this regard, the method proposed herein not only constitutes state-of-the-art direct particle image segmentation, but it also offers an excellent tool for generating such datasets that can be used for yet-to-be developed CNNs.

Moreover, a key component of proper phase separation is the identification of the shapes and locations of the phase boundaries (*i.e.*, *interfaces*) to a high degree of accuracy. For instance, in multiphase flow in porous media, the dynamic detection of fluid–fluid interfaces is not only critical for tracking fluid phase migration [6], but also key to understanding many heat, momentum, and mass transfer processes, including shear, dissolution, exsolution, and chemical reactions [13, 14, 21, 22, 23]. Even for flows not involving porous media, such as inhomogeneous turbulent flows, flames, and turbulence-non-turbulence transitions, interface detection in PIV images with sub-pixel accuracy can provide extremely valuable information about diffusion properties and turbulent mixing [24, 25].

A common way to track fluid–fluid interfaces is to tag one or more fluid phases uniformly with a contrast agent *e.g.*, molecular dyes). In this case, phase separation can first be achieved by means of either color or intensity discrimination. This approach is widely adopted in X-ray micro-computed tomography (micro-CT) [26] where a contrast agent is sometimes used to enhance intensity differences between phases[27, 28, 29]. In these images, since the bulk of a phase is uniformly tagged, interfaces (*i.e.*, strings of pixels) can be obtained via simple thresholding and edge detection based on grayscale values or gradients of grayscale values. However, this method is not amenable to quantification of velocity distributions due to the absence of particle tracers that faithfully follow the fluid motion. In PIV applications, *discrete* neutrally buoyant particles are conveniently introduced in the flow as shown in Fig. 1. The motion of the particles is tracked by robust image interrogation algorithms. Particle seeding density can vary depending on the specific tracking algorithm to be used and on the targeted spatial resolution of the resolved flow. At the highest level of tracer seeding in μPIV, pixels corresponding to particles occupy no more than 25% of the total image area [4].

Manual detection of continuous interfaces using discrete particle images similar to that shown in Fig. 1 is relatively easy, even for low seeding densities, due to the manner in which the human brain processes these images and is able to "connect the dots". However, manual detection is user-dependent, time-consuming and often impractical for experiments involving large datasets and/or high-speed imaging [11, 30].

In contrast, interface detection tasks from images of dispersed particles are challenging to computer algorithms due to the discrete nature of the information. These tasks require prediction and space-interpolation abilities that are surprisingly non-trivial to canonical image analysis tools. Intensity-based segmentation has been relatively successful, where a typical four-step image processing sequence was proposed [16, 31]: (*i*) median filtering to even out grayscale values, (*ii*) thresholding to create a binary image, (*iii*) several rounds of image dilation and erosion to close the gaps between particles, and (*iv*) edge detection in the binary image to locate the interfaces. Ergin [16] successfully used this approach to separate a moving object in a fluid flow with acceptable errors reported in the vicinity of the object edge. Carrier et al. [31] was able to apply this approach to study water droplet formation in an oil phase, with water and oil being seeded and unseeded with tracers, respectively. However, during image dilation and erosion cycles, the interface shapes were not very well preserved, leading to undesirable artifacts in the measurement [5, 31]. Alternatively, direct boundary detection methods aim to directly determine the locations of the interfaces based on the gradients of the intensity or even more advanced algorithms, and can therefore yield more precise results. This method has been successful in tracking a flame front in PIV measurements of a turbulent premixed flame [32] as well as in free surface flows where the phase boundaries are identified by light reflection/refraction or the seeding particles floating at the free surface [33, 34, 35, 36]. The drawback of this method, however, is that it is only applicable when distinct boundary lines (*e.g.*, due to light reflection/refraction) exist between phases, which is not always satisfied, as highlighted in the examples reported in Fig. 1a. More recently, studies have reported successful identification of interfaces in PIV images based on the spatial distribution of tracer particles in the fluid domain [37, 38].

In certain applications, it is impractical to use different tracer particles for each phase or region of the flow, and therefore color or intensity-based discrimination methods are not effective. Instead, seeding more than one phase or region with the same tracer particles is often convenient and might be the only suitable option in certain cases. For instance, in inhomogeneous turbulence caused by a single-phase mixing jet and in turbulent flames, where the fluid phases are miscible and the interface only persists within the mixing time scale, particle seeding density is the most, if not the only, suitable differentiator between phases. For these cases, phase discrimination and interface detection must be obtained more conveniently by controlling the *particle seeding density* for each phase or region [25, 24]. As an example, Gan [24] estimated scalar interfaces directly from conditioned PIV images of a jet and a vortex ring based on the particle seeding density difference in the area of interest (see Fig. 1b).

A wavelet-based thresholding method, which selectively retains large-scale features while eliminating small-scale details was applied to enhance the contrast between the particle images in each phase in order to aid the interface detection. Pfadler et al. [25] previously employed a similar method to detect flame fronts in turbulent premixed flames, where the seeding density is higher before combustion, and lower afterwards due to a sudden expansion of gases. To distinguish between unburnt and burnt regions, intensity thresholding was applied to the particle images following spatial filtering. In both studies, although the seeding density is used as the differentiator, its difference between phases was essentially transformed into a difference in grayscale values, which, due to high susceptibility to illumination nonuniformity, may limit accuracy.

In summary, image segmentation is crucial in many PIV applications, yet no existing segmentation method achieves desirable levels of practicality and accuracy, thus often requiring users to over-complicate their setup. Specifically, for the μPIV application to study immiscible multiphase flow in porous media (see Fig. 1a), none of the aforementioned techniques are able to produce accurate and consistent results. To that end, a novel and robust method for phase separation and interface identification in PIV images based on seeding density differentiation through robust particle detection and triangular meshing is presented. The first step involves particle identification throughout the whole domain. The coordinates of the particles are then used to construct a 2D unstructured mesh. This mesh possesses different characteristics in each phase due to the average particle distance, providing the basis for phase separation and fluid–fluid interface detection.

2. Algorithm and Implementation

The image processing protocol developed herein consists of six well defined steps, as summarized in the flow chart in Fig. 2: (1) Particle detection; (2) Mesh generation; (3) Thresholding of edge length; (4) Surface node detection; (5) Curve fitting; (6) Mapping mesh to a segmented image.

To demonstrate the working principle and image processing procedures of the proposed method, a synthetic image as shown in Fig. 2a is created in MATLAB, where two regions with dense and sparse particles represent the high and the low seeding-density regions, respectively. The two regions are divided by a curved interface. In step 1, individual particles are detected throughout the entire image (Fig. 2b). This is achieved by identifying candidate particles by the brightest connected pixels within small regions of approximately the expected size of one particle in the image. This can be estimated based on the actual particle size, lens performance and size of a camera pixel. For each candidate particle with an estimated location $(x_\circ, y_\circ)$, its corrected location (x_i, y_i) with sub-pixel accuracy is determined by computing the centroid-weighted position as

$$(x_i, \quad y_i) \quad = (x_\circ, \quad y_\circ) \quad + \frac{1}{M} \sum_{i^2+j^2 \leq w^2} (i, \quad j) \quad I(x_\circ + i, y_\circ + j) \quad (1)$$

and

$$M = \sum_{i^2+j^2 \leq w^2} I(x_\circ + i, y_\circ + j), \quad (2)$$

where w is a preset integer larger than the radius of one single particle, but smaller than the average spacing between particles, and M is the integrated grayscale value

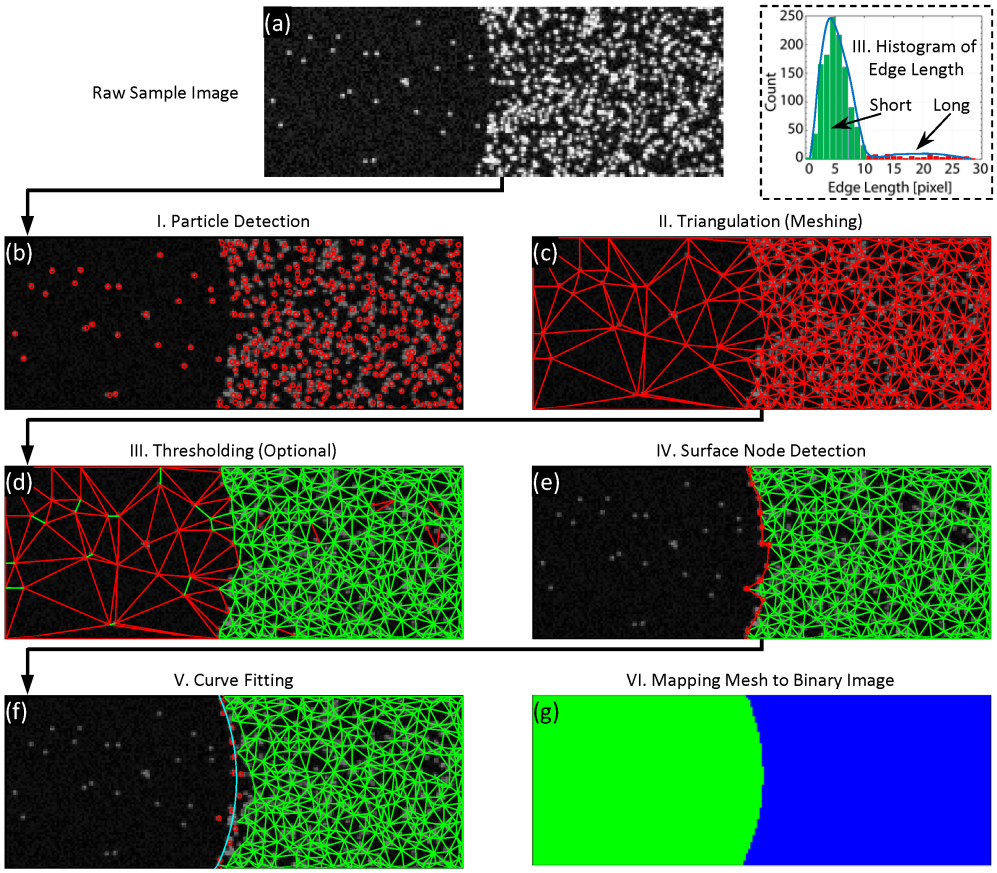

Figure 2. General flow chart illustrating the working principle and major steps of the particle-based image segmentation method for phase separation and interface detection.The inset on top right shows the histogram of the lengths of the edges as shown in step II, which helps determine a threshold to be used in step III. (for interpretation of the references to colors in the text, the reader is referred to the web version of this article.)

of the particle image [39]. In this step, depending on the quality of the images, pre-processing such as band-pass filtering and/or background subtraction can help improve efficiency and accuracy of particle detection.

In step 2, the coordinates of the detected particles are used to construct an unstructured mesh using a triangulation algorithm, so that each particle is linked to its nearest neighbors. The length of the mesh edge connecting a particle to its neighbor is essentially the distance between them. Each edge length is used as a metric to infer the local seeding density, with long edges statistically more likely to belong to low seeding-density regions and short edges to high seeding density.

In step 3, shorter edges are separated from longer edges by selecting an appropriate threshold that reflects the seeding density of each phase. A histogram of the edge lengths across the entire image typically features a bimodal distribution separated by an inflection point, as shown in the inset in Fig. 2, which is the real histogram generated based on the edges plotted in Fig. 2c. The position of this inflection point yields a reasonable estimate of the threshold (*i.e.*, 10 pixels in this case). The result of the histogram-guided thresholding operation is shown in Fig. 2d where edges with lengths above and below the threshold are shown in red and green, respectively. This operation reveals extended regions in which particle density appears consistent, with only a few outliers. The boundary between these two regions represents the interface between the phases. The outlier edges are due to the crosstalk between the PDFs of the high and low-seeded regions. The outliers in the low seeding-density region tend to be more numerous than those in the high seeding-density region and result from two particles that are accidentally closer than average. The outliers in the high seeding-density region are due to holes in the seeding distribution, caused by uneven seeding. In most cases the outlier edges can be easily identified using a combination of local filters based on edge connections and neighbor analysis. In particular, once the longer edges are eliminated, the outlier edges are typically not associated with any triangles, which helps to identify and eliminate them. It is worth noting that, while a certain amount of crosstalk is unavoidable, the higher the seeding density difference between the two regions, the more negligible the crosstalk is. An analysis performed on synthetic images (not shown for brevity) revealed that density ratios higher than 10 : 1 are ideal for the method presented herein using automatic thresholding. For lower density ratios, the method begins to fail frequently, and may not be appropriate. For images obtained experimentally, especially those impacted by uneven seeding and illumination density, some level of manual input and trial and error may be needed to fine-tune the threshold for specific experimental settings. An analysis on how uneven illumination affects the accuracy of the results obtained by this method is provided in § 3.4. Note that the thresholding step is only necessary if both regions are seeded. However, for the scenario where only one phase is seeded, performing this step would help remove noise and potential stationary particles contaminating the region occupied by the unseeded phase.

In step 4, interfacial elements (*i.e.*, edges and nodes) are identified by recognizing that interfacial edges belong to a single element (*i.e.*, triangle), whereas internal edges are shared by two elements. All interfacial edge ends are defined by two interfacial nodes. Once the interfacial nodes are determined, in step 5 a curve is fitted using a proper function form to help improve the interface shape and location. A proper fitting function form can often be determined based on fundamental knowledge of the flow and interfacial dynamics under study. For example, in multiphase flow in 2D microchannels, the interface shape is an arc, thus curve fitting to a circle is a reasonable approximation. In other cases, such as a flame front and in turbulent mixing, complex functional forms such as polynomials or more sophisticated fitting schemes can be used. Finally in step 6, the meshed regions divided by the fitted interfaces are labeled separately, which completes the image segmentation and interface detection process.

The algorithm described herein was implemented in MATLAB. Particle detection was achieved employing a subroutine adapted from a PTV code [39], and the unstructured mesh was generated employing a built-in routine in MATLAB called "delaunayTriangulation". Delaunay triangulation is used herein because it is, in our opinion, one of the most effective and established tools to determine a particle-based triangulation network corresponding to precise mathematical rules and, from that, the distances between a particle and its neighbors. The edges of the triangulation serve as a direct metric for identifying local particle seeding density. While other algorithms such as Voronoi tessellation will likely yield similar results, Delaunay triangulation is chosen to facilitate its implementation and subsequent thresholding

Table 1. Synthetic image conditions and nomenclature.

e (pix^{-1})	d (pix)						
	1	2	3	4	5	6	7
1/160	A1	A2	A3	A4	A5	A6	A7
3/160	B1	B2	B3	B4	B5	B6	B7
5/160	C1	C2	C3	C4	C5	C6	C7
7/160	D1	D2	D3	D4	D5	D6	D7
9/160	E1	E2	E3	E4	E5	E6	E7
11/160	F1	F2	F3	F4	F5	F6	F7
13/160	G1	G2	G3	G4	G5	G6	G7
15/160	H1	H2	H3	H4	H5	H6	H7
17/160	I1	I2	I3	I4	I5	I6	I7

step [40]. Alternative triangulation methods may produce similar results. (Testing the performance of different triangulation is beyond the scope of this manuscript.) Curve fitting and image pre-/post-processing were performed using the Curve Fitting Toolbox™ and the Image Processing Toolbox ™, respectively, in MATLAB.

3. Validation and Error Quantification

The proposed method was validated using synthetic particle images. This approach has several advantages. In addition to the ability of controlling image parameters such as particle size and density, using synthetic particle images provides a ground truth for the phase distribution and interface location. Therefore, this validation method allows for a parametric quantitative evaluation of the accuracy of the method. Following a previous study [24], the primary metric for such evaluations is based on the root mean square error ($RMSE$) between the calculated and the true data, defined as

$$RMSE = \sqrt{\frac{1}{N}\sum_{i=1}^{N}(X_i - X_i^*)^2}, \tag{3}$$

where X_i and X_i^* are the calculated and the true interface locations, respectively.

3.1. Synthetic particle image generation

The synthetic images created herein contain two regions, with the left region sparsely or not seeded with tracer particles, and the right one seeded at much higher density. To generate such an image, a dark 8-bit image (*i.e.*, matrix of zeros) of 200 × 200 pixels was first created. Meanwhile, a virtual interface with a known x coordinate for each y position was pre-defined. Following this, randomly distributed particles were added to the region that is to the right of the virtual interface. The intensity of a particle was set to follow a Gaussian profile across its diameter, and the maximum grayscale value was 190 (out of 255). The two parameters of interest are the size of an individual particle, d and the seeding density, e. For this evaluation, a total of

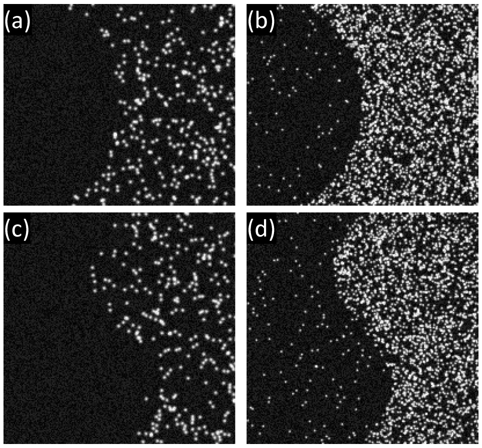

Figure 3. Representative synthetic images used to evaluate the method. (a) Image with an arc-shaped interface and one phase seeded with $d = 5$ pixels and $e = 3/160\,\mathrm{pixel}^{-1}$; (b) Image with an arc-shaped interface and both phases seeded with $d = 3$ pixels and $e = 1/160\,\mathrm{pixel}^{-1}$ and $e = 1/8\,\mathrm{pixel}^{-1}$, respectively; (c) Image with an sinusoidal-shaped interface and otherwise identical to (a); (d) Image with an sinusoidal-shaped interface and otherwise identical to (b).

63 different combinations of d and e were tested within the bounds $1 \leq d \leq 7$ pixels (with an increment of 1 pixel) and $1/160 \leq e \leq 17/160\,\mathrm{pixel}^{-1}$ (with an increment of $2/160\,\mathrm{pixel}^{-1}$), as summarized in Table 1. Particle seeding density here is defined as the number of particles per unit area denoted in pixels. For the first 63 cases, only the region to the right of the interface is seeded through one round of particle generation. However, to test the capability of the method to segment based on particle seeding density, in two extra cases as shown in § 3.3, a second round of particle generation is performed to add particles to the entire image, creating a contrast of seeding density between the two sides of the interface. The minimum seeding density ratio tested is approximately 1 : 10. In addition, random noise with an average grayscale value of 30 was added the the background on top of the particle-image intensities. Finally, for each combination of particle size and seeding density, two different interface shapes, an arc and a sinusoid, were tested. Although the methodology described here is not restricted by the interface shape, μPIV measurements of multiphase flow in 2D micromodels serve as the impetus for this method development, where the projected fluid–fluid interfaces are arcs. A few representative synthetic images are shown in Fig. 3 that are meant to reflect typical scenarios of in porous media (*e.g.*, air–water flow in where only water is seeded, Fig. 3a; oil–water flow, where both phases are seeded at different seeding densities, Fig. 3b).

3.2. Segmentation of seeded from unseeded regions

Following the procedures outlined in §2 and Fig. 2, the synthetic images were processed and the $RMSE$ value was calculated for each case. As a baseline for comparison, the same set of images was also processed using the intensity-based segmentation method, which consists of four standard steps: (*i*) median filtering, (*ii*) intensity thresholding, (*iii*) image dilations and erosions, and (*iv*) edge detection [16, 31]. Additionally, the proposed particle-based segmentation method includes a curve fitting step. Therefore,

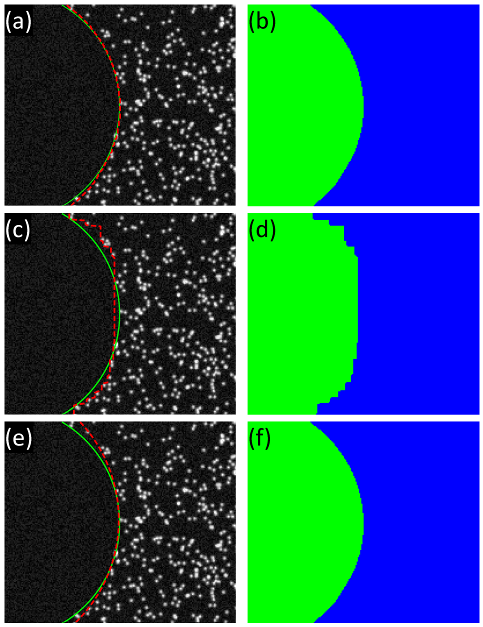

Figure 4. A synthetic image (*i.e.*, case B5) processed with three different schemes: (a,b) particle-based segmentation; (c,d) intensity-based segmentation *without* curve fitting and (e,f) intensity-based segmentation *with* curve fitting. The green and red curves plotted in the left column demarcate the locations of the true and detected surfaces, respectively, and the right column shows the final segmented images.

to ensure a fair comparison between the two different methods, a curve fitting was also performed in the intensity-based segmentation method as a fifth step, which, as shown in Fig. 4e, always helps to improve the segmentation accuracy of the interface detection. For example, the same synthetic image (*i.e.*, case B5 as defined in Table 1) was processed with three different schemes and the comparative results are presented in Fig. 4: (a,b) particle-based segmentation; (c,d) intensity-based segmentation *without* curve fitting and (e,f) intensity-based segmentation *with* curve fitting. The green and red curves in this figure demarcate the locations of the true and calculated interfaces, respectively, and the right column shows the final segmented images. The $RMSE$ values for the three cases are 1.98 pixels (particle-based segmentation), 5.75 pixels (intensity-based segmentation *without* curve fitting) and 4.73 pixels (intensity-based segmentation *with* curve fitting). As such, for this illustrative test, the particle-based method yields the best performance, while the curve fitting step in the intensity-based method aids its accuracy. Therefore, curve fitting is performed by default for all cases in what follows unless otherwise specified.

Figure 5 presents $RMSE$ values as a function of particle seeding density and particle size for all 63 cases described in §3.1 (see Table 1) using both the particle-based method (*c.f.*, Fig. 5a) and the intensity-based method (*c.f.*, Fig. 5b). These synthetic images feature interfaces of an arc shape, again inspired by our previous work investigating multiphase flow through idealized porous media [41]. It is seen in Fig. 5a that $RMSE$ associated with the particle-based method decreases with increasing seeding density, from a range of $RMSE = 1.5 - 4.6$ pixels at $e = 1/160\,\text{pixel}^{-1}$ to

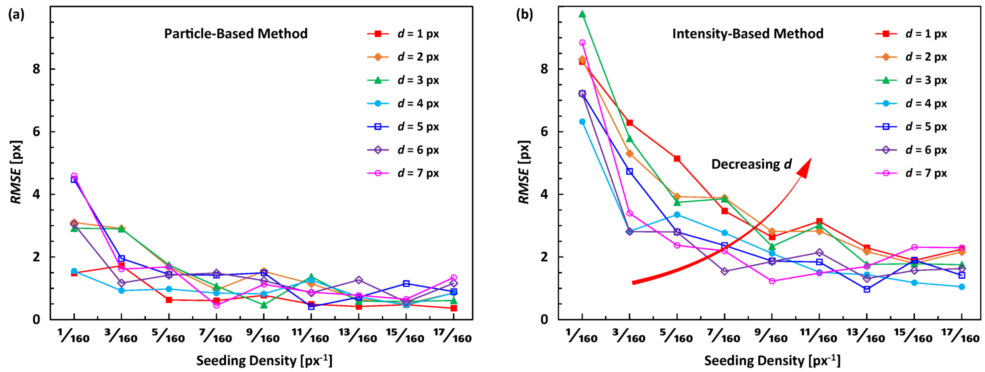

Figure 5. $RMSE$ values as a function of particle seeding density and particle size for all the 63 cases as described in Section §3.1 using both the particle-based method (a) and the intensity-based method (b). The synthetic image feature interfaces of an arc shape.

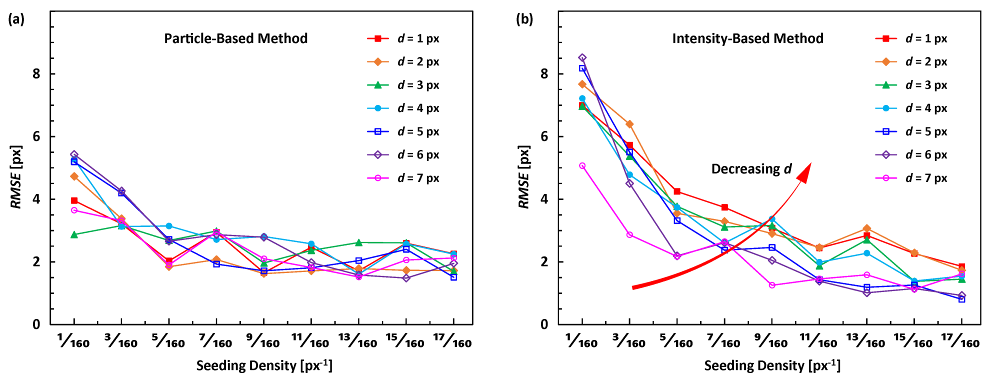

Figure 6. As in Fig. 5, but with a sinusoidal-shaped interface.

$RMSE = 0.4 - 1.5$ pixels at $e = 17/160\,\text{pixel}^{-1}$. This trend is expected, as a higher seeding density simply implies more information as to the interface location, which results in more data points for curve fitting and therefore more accurate determination of the interface. These results also reveal that the particle-based method $RMSE$ is quite insensitive to variation in particle size, as no apparent trend is observed in $RMSE$ for the range of particle size assessed. This insensitivity is likely because the particle-based method is primarily based on the locations of individual particles. As such, once a particle is located, its size becomes unimportant and location accuracy is directly linked to the ability to properly identify its centroid. Low sensitivity to particle size is thought to be an important advantage of this method, especially for applications where particle size cannot be easily controlled. As a comparison, Fig. 5b shows the results obtained under otherwise identical conditions using the intensity-based method. Immediately, it is seen that the $RMSE$ values are much higher than those of the particle-based method, especially when both particle size and seeding density are low. The highest $RMSE$ value observed is as large as 9.8 pixels. Additionally, $RMSE$ is highly dependent on seeding density as well as the individual particle size when the intensity-based method is employed. This sensitivity is to be expected, since the accuracy of the intensity thresholding and morphological operations (*i.e.*, dilations and erosions) highly depends on the *area* of the thresholded regions, to which both particle size and seeding density can contribute.

Figure 6 presents trends of $RMSE$ for the particle-based and the intensity-based methods for synthetic images with *sinusoidal* interfaces. A sixth-order polynomial is utilized for curve fitting purposes. Again, compared with the intensity-based method, the particle-based method performs significantly better, especially for low-seeding-density and low-particle-size cases, whereas similar performance was achieved between the two methods when both particle size and seeding density are high. For both methods, the $RMSE$ value decreases as the particle seeding density increases. While the $RMSE$ is relative insensitive to particle size when using the particle-based method, it drastically increases with decreasing particle size using the intensity-based method (Fig. 6b).

It is noteworthy that the results in Figures 5 and 6 do not show smooth trends but instead present fluctuations from one case to the next. This behavior is likely due to the fact that particle locations in the synthetic images are all randomly generated, with some locations favoring the curving fitting better than others. In other words, even for two synthetic images generated independently with the same seeding density and particle size, the results would still be slightly different due to the random arrangement of particle locations. In that sense, the $RMSE$ of each case can be attributed to two categories of error sources, namely random error and systematic error (bias). The former includes but is not limited to uncertainties in particle detection and the random spatial distribution of particles; the latter includes conditions often unavoidable in experimental images, the most common of which is an uneven illumination, resulting in uneven particle density within the same phase. In the case of the synthetic images used for this analysis, a source of systematic error may also be introduced by the specific fitting curve used. Both of these errors are expected to depend on the seeding density. In an effort to isolate and quantify the random error from the total $RMSE$, a statistical analysis on synthetic images was conducted for different seeding densities. A single particle size ($d = 3$ pixels) and a full particle density range were considered in this analysis (*i.e.*, cases A3 - I3 shown in Table 1). For each particle density, 30 synthetic images were generated, each with a different randomly generated particle distribution [38]. The $RMSE$ value of each individual image was calculated, which represents the total $RMSE$. Figure 7 presents a box plot that shows the contributions of the random error and systematic error to the overall $RMSE$. For each seeding density, the $RMSEs$ of 30 cases each with randomly distributed particles are shown. While the average $RMSE$ of all 30 cases represents the systematic error for each condition, the box size represents the random error caused by the random spatial distribution of particles, which is about 50% of the average $RMSE$.

3.3. Segmentation based on seeding density

A primary advantage of the particle-based method is that it enables image segmentation and interface detection based on differences in particle seeding densities between different fluid phases (*i.e.*, average distances between particles). This scenario proves challenging with other techniques like the intensity-based method. To verify this ability, two sets of synthetic images were created and processed as shown in Figs. 8 and 9. Figure 8a shows a raw synthetic particle image where two fluid phases are seeded with particles with $d = 3$ pixels at $e = 1/160\,\text{pixel}^{-1}$ and $e = 10/160\,\text{pixel}^{-1}$,

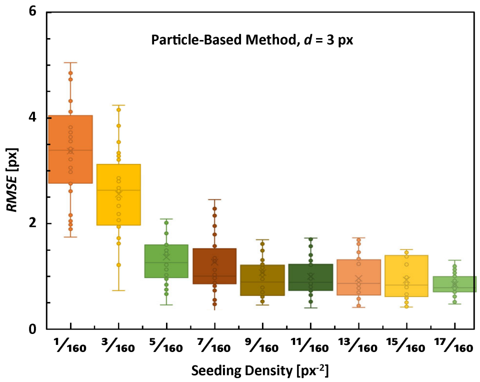

Figure 7. Boxplot presenting the relative contributions of the random error and systematic error to the overall $RMSE$ for $d = 3$ pixels. The $RMSEs$ of 30 cases, each with randomly distributed particles, are shown. The average $RMSE$ represents the systematic error for each condition. The box size represents the random error caused by the random spatial distribution of particles.

respectively, yielding a seeding density ratio of 1 : 10. The two fluid phases are divided by an arc-shaped interface. The resulting particle-image detection shown in Fig. 8b highlights the fact that the phase to the right of the interface has a much higher seeding density. Figure 8c presents the triangulation based on the detected particles and thresholded edges with longer and shorter edged denoted in blue and green, respectively, while the calculated interface is shown in red. In this specific case, a length threshold of 13 pixels was used. It is worth noting that in real experiments, this threshold must be carefully selected based on the specific experimental configurations and the histogram of edge length as demonstrated in Fig. 2d. Figure 8d presents the completed segmentation, and the true interface is indicated by the red dotted line. In this case, the $RMSE$ between the detected and the true interfaces is 1.2 pixels. Figure 9 shows similar results, but for a case with a sinusoidal interface between the two phases (all other parameters are identical to that of Fig. 8). For this sinusoidal interface, the $RMSE$ of the detected interface is 1.6 pixels with an edge length threshold of 12 pixels.

It is noteworthy that, like many other existing methods [24, for example], the particle-based method is also restricted by the particle seeding density contrast (*i.e.*, ratio) between the fluid phases, with higher contrast much favored. In the present work, the lowest contrast that yields acceptable results is 1 : 10. With decreasing seeding density contract, the algorithm fails frequently to detect the interface with an acceptable accuracy. Nevertheless, this method provides a novel and alternative way to perform image segmentation and interface detection, and it works particularly well for multiphase flow scenarios where one phase is sparsely seeded (*e.g.*, for PTV measurement), and a second phase is densely seeded (*e.g.*, for PIV measurement) as is often the case in studies of porous media flows. Other potential applications include flame front tracking and inhomogeneous turbulent flow as mentioned previously.

3.4. Effects of uneven illumination

PIV images obtained experimentally often suffer from imperfections that can introduce bias in the detection of the interface. The most common of these conditions

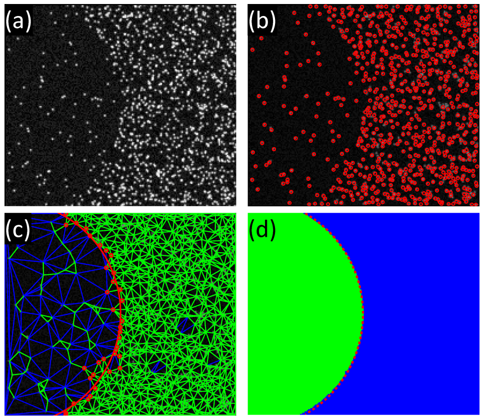

Figure 8. Image segmentation and interface detection of a synthetic image based on distinct particle seeding densities in different phases: (a) raw synthetic image; (b) particle detection in the entire image; (c) thresholding based on particle distances, with longer and shorter edges denoted in blue and green, respectively; and (d) segmented image with the left and right phases denoted in blue and green, respectively, and the true interface of an arc shape indicated by the dotted red line. The seeding density ratio between the two phases is $1:10$, and the $RMSE$ of the detected interface is 1.2 pixels.

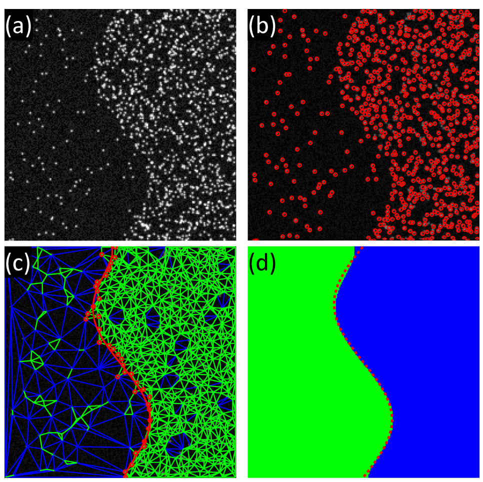

Figure 9. As in Fig. 8, but for a sinusoidal-shaped interface. The seeding density ratio between the two phases is $1:10$, and the $RMSE$ of the detected interface is 1.6 pixels.

is uneven illumination of the field of view. While the particle-based method is relatively insensitive to uneven illumination, compared to intensity-based methods, this condition may still result in particles being under detected in low light regions, thus affecting the triangulation accuracy. To quantify the sensitivity of our specific method to illumination gradients, a controlled analysis based on synthetic images was performed. Gradient filters were applied to the same synthetic image that is presented in Fig. 8 to mimic the effect of a fading illumination. The goal of the analysis was to generate a series of images with the same particle size and seeding density, but

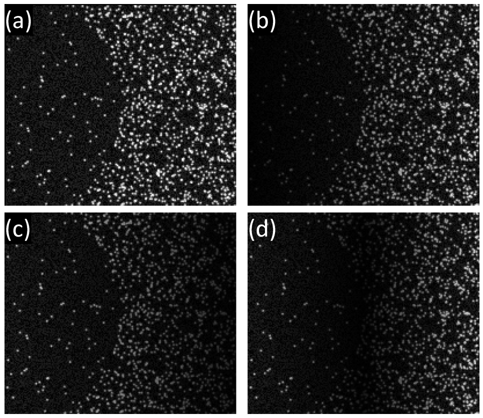

Figure 10. Representative synthetic images used to evaluate the impact of intensity non-uniformity. (a-d) present the original image, an image with a dark low-seeded region, an image with a dark high-seeded region, and an image with a dark interface, respectively.

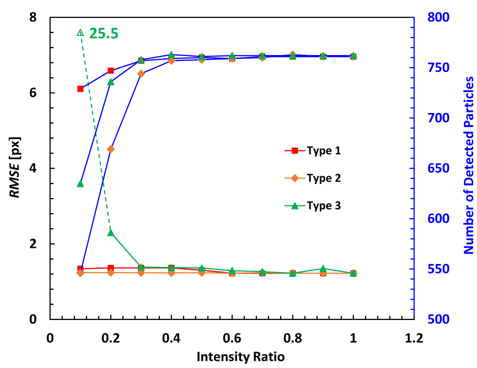

Figure 11. $RMSE$ values and number of detected particles as a function of intensity ratio. An intensity ratio of 0.1 indicates the most severe intensity non-uniformity, whereas an intensity ratio of 1 indicates no intensity non-uniformity. The blue curves are plotted relative to the right axis.

with artificially introduced intensity non-uniformity using horizontal gradient filters. Figure 10 presents the original image (a) and three variations of it featuring (b) Type 1, a darker low-seeded region, (c) Type 2, a darker high-seeded region, and (d) Type 3, a dark interface, respectively. As an example of this gradient filter application, a 2D matrix of the original image size was first generated so that its element values varied linearly from 0.1 in the first column to 1 in the last column to generate the image in Fig. 10b. The matrix was then multiplied with the original image, so that the intensity of a particle on the left edge of the modified image decreased to 10% of its original value while the intensity of a particle on its right edge remained unaltered. The other two types of non-uniformity were created in the same way but with different directions of the intensity gradient. For each type, the severity of the non-uniformity was varied by changing the power of the filter, which was identified by the parameter Intensity Ratio, IR. Ten different intensity ratios were considered for each type of non-uniformity with $0.1 \leq IR \leq 1.0$.

The modified images were then processed using the particle-based method and the results are shown in Fig. 11. As expected, as the non-uniformity becomes more severe the number of detected particles progressively decreases for all cases considered. However, the results indicate that the $RMSE$ is relatively unaffected by even large non-uniformity with one apparent exception for the Type 3 case. The results show that for $IR < 0.3$ the detection method clearly fails due to the interface becoming extremely dark.

4. Application: Multiphase flow of liquid CO_2 and water in a 2D porous micromodel

The development of this methodology was inspired by on-going high-speed μPIV measurements of liquid CO_2–water multiphase flow in 2D porous micromodels, which is of fundamental importance in geologic CO_2 sequestration as well as EOR and ground water remediation [7, 8]. In brief, the goal of such studies is to quantify the pore-scale flow of water and liquid CO_2 as well as the dynamics of the interface between these two immiscible fluid phases in 2D micromodels (For more details on such efforts, the reader is referred to refs. [11, 12, 13, 14, 42, 43, 6, 15].). Success in this regard requires accurate identification and tracking of the interface within the flow domain imaged. Sample data from this research effort are presented in this section to confirm the fidelity of the particle-based image segmentation method using real experimental data (as opposed to the previous assessment in §3 using synthetic images). A short summary of the apparatus and experimental approach is given below, and the reader is referred to refs. [12, 13, 14, 42, 43, 6] for additional details.

4.1. Experimental apparatus

Micromodel The 2D porous micromodels used in this study were fabricated from a silicon wafer using standard micro-fabrication techniques [44, 12]. Each micromodel is of a circular shape with the inlet port located in the center and the outer edge open serving as the flow exit, as shown schematically in Figs. 12b,c. The porous section consists of randomly-distributed poly-dispersed cylindrical posts whose layout was generated based on an irregular mesh inside a circle using the pdemesh tool in Matlab [45]. Based on the designed pattern, sequential processes involving standard photolithography, inductively coupled plasma-deep reactive ion etching (ICP-DRIE) and Piranah cleaning were used to create the cylindrical structures. The contact angle of water on both surfaces was estimated to be $\sim 9 \pm 1\,^\circ$ using CO_2 as the non-wetting phase under actual experimental conditions. Finally, two nanoports (IDEX Health & Science) were attached to the micromodel for fluid delivery. The completed micromodel has internal dimensions of $(D, h) = (10, 0.030)$ mm and a porosity of $\varepsilon = 0.44$. The cylidrical posts extended from the base to the top of the micromodel, ensuring 2D flow through the porous system.

Flow system The experiment was performed using distilled water and CO_2 as the working liquids at 8 MPa and 21°C by employing an overburden pressure cell. The water phase was seeded with fluorescent polystyrene particles of 1μm diameter (Invitrogen F8819), at a nominal volume fraction of 3×10^{-4}. Only the water phase was seeded owing to challenges in identifying appropriate tracer particles for liquid CO_2. As such, only the water-phase velocity field was quantified via μPIV measurements

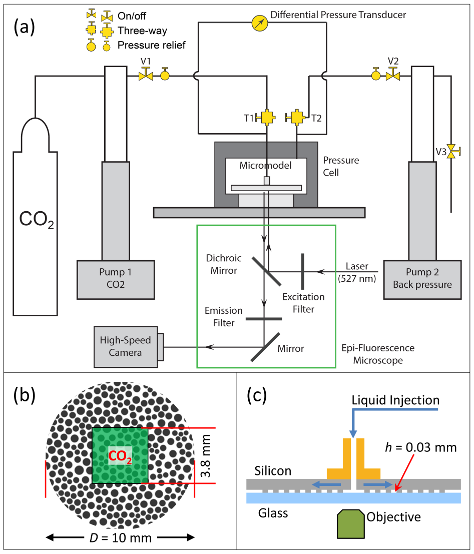

Figure 12. Schematic diagrams depicting (a) the apparatus; (b) the micromodel with the imaging field of view noted in green; and (c) the flow configuration through the micromodel in side view.

[12, 41]. The coupled flow of water and CO_2 through the micromodel was controlled by two high-pressure syringe pumps (Teledyne Isco 100DM), as shown schematically in Fig. 12a. Pump 1 was used to push the liquid CO_2 into the micromodel through the inlet, while pump 2 was used to withdraw the resident water from the outlet as well as to maintain the back pressure. Prior to each experiment, the CO_2 in Pump 1 was pressurized to 8 MPa and allowed to equilibrate at room temperature for over 2 hr. Meanwhile, the micromodel was mounted in the overburden pressure cell, which was then filled with distilled water under ambient conditions. As the circumferential edge of the micromodel is open on the outer edge, it was automatically pre-saturated with distilled water after the pressure cell is filled. The micromodel port and the pressure cell port were then connected to Pumps 1 and 2, respectively, and both pressurized to 8 MPa with valve V1 closed (see Fig. 12a). After the pressure on the water and CO_2 sides reached equilibrium, valve V1 was opened and the CO_2 and water pumps were simultaneously initiated to run at the same flow rate of 5×10^{-3} ml/min, each with an accuracy of 0.3% of the setpoint. See refs. [11, 12, 13, 14, 6] for more information on this experimental approach.

Image acquisition To image the flow, a high-speed dual-head frequency-doubled Nd:YLF laser (Litron LPY300) with a wavelength of 527 nm was used to excite the fluorescent particles seeded in the water phase. The fluorescence emitted from the tracer particles was passed through a $\lambda = 575 \pm 13$ nm bandpass filter (Semrock BrightLine FF02-575/25-25) and focused by an Olympus IX-73 microscope equipped with an objective lens with 4$\times$ magnification and 0.1 numerical aperture (NA), onto the detector of a high-speed scientific CMOS camera (Phantom v641). The resultant depth of field is 55 μm, and the field of view was approximately 3.75×3.75 mm, as indicated by the green region in Fig. 12b. In order to capture the high-speed flow

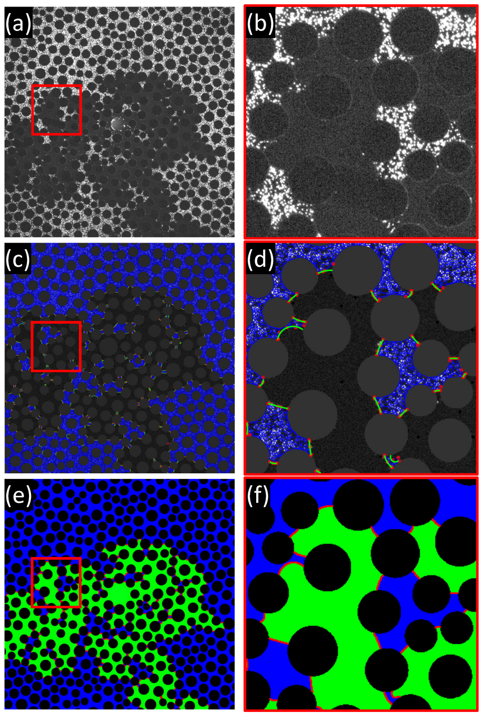

Figure 13. Particle-based segmentation of a representative particle image from μPIV measurements of water–CO_2 multiphase flow in a 2D porous micromodel. (a,b) A raw experimental image with the water phase occupying the region filled with bright particles and the CO_2 phase occupying darker regions of the image domain (the cylindrical posts appear as black regions); (c,d) Triangulation and detected interfaces plotted in blue and green, respectively; (e,f) The segmented images, with water, CO_2 and the interfaces shown in blue, green and red, respectively. Left column: entire field of view; Right column: Zoomed-in views of the regions enclosed by red squares in the left column.

dynamics, a "frame straddling" scheme was used where frame pairs were acquired at 500 Hz. The exposure time of each frame is determined by the duration of the laser pulse, which is $\sim$10 ns. The effective time interval between the two image frames within one pair was set to $\Delta t = 500\,\mu$s, by adjusting the delay between the two laser pulses.

4.2. Image processing

Image segmentation and interface detection of the experimentally-acquired images were achieved by employing the aforementioned particle-based method. Thanks to the utilization of high-speed imaging, each set of data depicting a complete flow process in one experimental run consisted of 3800 PIV image pairs, with each pair requiring one mask. As such, particle-based image segmentation and interface detection were applied to the first frame within each image pair.

Each raw PIV image (Fig. 13a,b) was first preconditioned by subtracting a "minimum image" from it. A "minimum image" of an image set is defined such that each pixel is assigned with the temporally minimum grayscale value to have appeared

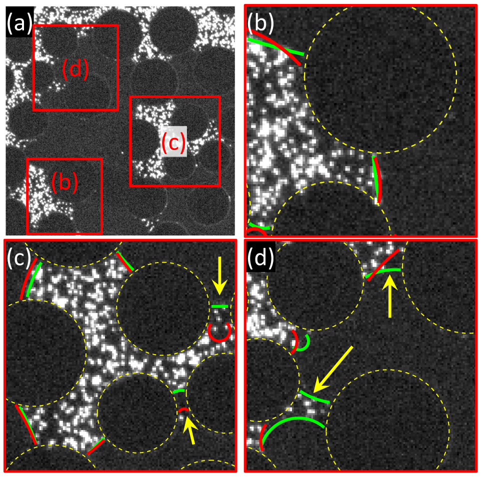

Figure 14. Comparison of particle- and intensity-based methods on experimental images. (a) A region of a representative raw experimental image (same as in Fig. 13b); (b–d) zoomed-in views of the regions enclosed by the red squares in (a). The green and red curves plotted in (b–d) demarcate the locations of the detected interfaces using the particle- and intensity-based methods, respectively; yellow dashed circles indicate the locations of the circular posts forming the solid matrix. The yellow arrows in (c,d) denote the locations where the particle-base method worked well, but the intensity-based method failed due to a lack of particles.

for that location during image capture. Subtraction of the “minimum image” is a routine step in PIV image prepossessing, as it effectively removes the background as well as stationary particles in a raw image. The images were then bandpass-filtered to further remove high-frequency noise and therefore enhance the signal-to-noise (SNR) of individual particles. The preconditioned images were passed through the particle detection algorithm with an estimate particle diameter of $w = 3$ pixels, which was comparable to the size of a real particle but smaller than the average distance between particles (step 1 in Fig. 2). Based on the coordinates of the detected particles, an unstructured mesh was constructed to link each particle to its nearest neighbors determined by the triangulation algorithm (Fig. 13c,d and step 2 in Fig. 2). In step 3, longer edges in the mesh were eliminated by applying a threshold of 16 pixels, which was determined by the histogram of the edge length distribution as explained in §2. As mentioned earlier, since only one (*i.e.*, water) of the two phases was seeded, the thresholding step was optional. However, performing this step helped to further remove any remaining stationary particles in the unseeded regions, which are usually far away from the majority of particles in the seeded regions. Following edge thresholding, interfacial edges and nodes were identified and curve fitting was performed using arcs to help improve the interface shape and location (Fig. 13c,d). Finally, the meshed regions were labeled separately from the unmeshed ones, divided by the detected interfaces (Fig. 13e,f).

To further highlight the ability of the particle-based method on real experimental images, the same image as shown in Fig. 13a was also processed using the intensity-based segmentation method. The results obtained using both methods are shown together in Fig. 14 wherein the green and red curves plotted in Fig. 14(b–d) demarcate the locations of the detected interfaces using the particle- and intensity-based methods, respectively, whereas the yellow dashed circles indicate the locations of the circular posts as the solid phase. Through visual inspection, it can be seen that both methods perform well and yield good agreement at locations where seeding particle are dense and large (*i.e.*, Fig. 14b, and the left half of Fig. 14c). However, when particles are sparse or stationary particle are present, the particle-base method still worked well, whereas the intensity-based method failed quite badly, as denoted by the yellow arrows in Fig. 14(c,d).

Once image segmentation and interface detection were successfully performed, the segmented regions with tracer particles (*i.e.*, water phase) were interrogated in the LaVision DaVis software, using a multi-pass, two-frame cross-correlation scheme to calculate the velocity field [12]. Unless otherwise specified, the sizes of the initial and final interrogation windows were 128^2 and 16^2 pixels, respectively, both with 50% overlap, which yielded a final vector spacing of 20 μm and spatial resolution of 40 μm.

4.3. Sample results

In this section, a few representative results are presented to demonstrate the efficacy of the particle-based segmentation method to process the actual PIV images of water–CO_2 multiphase flow in the circular 2D porous micromodel. The first benefit of the segmentation is that it directly provides high-quality dynamic masks for the subsequent PIV interrogation of tracer-particle movement in the water phase. Figure 15a presents an instantaneous velocity field depicting the water flow induced by the liquid CO_2 invading the micromodel with a constant flow rate of 5×10^{-3} ml/min. Figure 15b is a closeup view of the region enclosed by the red squares in Figure 15a. The arrows in these figures indicate the local water flow direction, while the pseudo-color contours demarcate the water velocity magnitude. These results illustrate the occurrence of a pore-scale burst event, known as a Haines jump [46], near the top-left corner of the field of view. This burst event induces very high speed flow in the vicinity of the water–CO_2 interfaces, which cause both fluids to migrate in an area within a few millimeters of this localize devent. In this regard, accurate automated phase segmentation and precise determination of the interface boundaries are crucial to spatially and temporally resolving pore-scale events like this, which evolve over several frames of the high-frame-rate PIV imaging. Alternatively, manually defining a new mask for each image pair would be impractical owing to the geometrical complexity of the interface and the shear size of the dataset. As such, this example is intended to demonstrate not only the fidelity of the particle-based segmentation method presented herein but also the value of the method for large datasets with significant levels of complexity.

In addition to facilitating automated dynamic masking for efficient PIV interrogation, the particle based-segmentation enables the study of aspects of CO_2 invasion into the micromodel, including evolution of CO_2 saturation and its interfacial length. The saturation of CO_2 in the field of view, S_{CO2} is defined as the ratio of the volume of the CO_2 phase inside the micromodel to the total pore volume of the micromodel, whereas the interfacial length is defined as the total projected length of the water–CO_2 interfaces, which is in turn often normalized by the total pore area to yield the specific interfacial length, A_{nw}. Figure 16a presents the variation of CO_2 saturation with injected pore volume, PV, which is a dimensionless number defined as the total volume of the CO_2 injected by the syringe pump normalized by the total pore volume (an equivalent proxy for time). Here, S_{CO2} grows roughly linearly

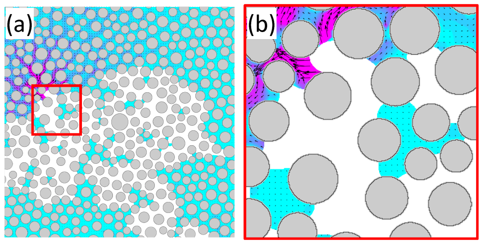

Figure 15. Instantaneous water velocity fields as CO_2 continuously displaces the resident water in the 2D porous micromodel. The arrows in these indicate the local water flow direction, while the pseudo-color contours demarcate the water velocity magnitude. The cylindrical posts of the porous micromodel are shown in gray, while regions occupied by CO_2 are shown in white.

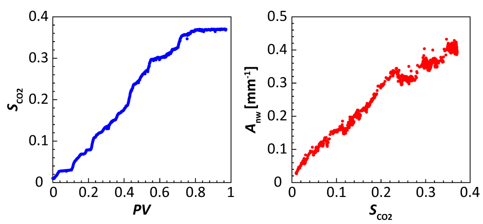

Figure 16. (a) Variation of CO_2 saturation as a function of injected pore volume, PV and (b) variation of the specific interfacial length with CO_2 saturation, highlighting the utility of the phase separation and interface detection of the particle-based method.

with PV though there exist significant deviations from this linear behavior where S_{CO2} grows much more rapidly with only small changes in PV. These incidences are interpreted as a reflection of the aforementioned bursting phenomena where the water velocity reaches very high magnitudes and CO_2 migrates rapidly through the porous domain. This behavior is also a reflection of the high compressibility of the liquid CO_2 under the current experimental conditions [41]. Figure 16b presents the variation of specific interfacial length with CO_2 saturation. When S_{CO2} is small, A_{nw} increases rather linearly with S_{CO2}, and as S_{CO2} get higher, the slope begins to decrease, consistent with previous results in rectangular micromodels [21, 6]. It is worth noting that, in theory, A_{nw} should go to 0 as S_{CO2} approaches 1, simply because there should no longer be any water–CO_2 interfaces when the entire porous section is fully occupied by the CO_2 phase. However, reaching a condition of $S_{\mathrm{CO2}} = 1$ is extremely challenging, as disconnected and trapped regions of water remain intact in the porous domain even after the CO_2 front has migrated through as illustrated in Fig. 15. These selected results highlight the rich physics embodied in this particular multiphase flow scenario that can be effectively analyzed when the interfaces between fluid domains can be accurately determined. The particle-based image segmentation method presented herein provides high fidelity in this regard.

5. Summary

A novel method for precise phase separation and interface identification in PIV images based on particle detection and triangular meshing is presented. Tracer particles in all seeded phases are first identified, and the coordinates of the particle locations are then used to construct a 2D unstructured mesh, where triangular grids provide a basis for phase separation and the outer edges provide a basis for interface detection. This method is particularly robust for processing PIV images and quantifying pore-scale flow and interface dynamics in multiphase flow in porous media, where the interface embodies a high level of complexity. While numerous techniques have been proposed to perform fluid-fluid and fluid-solid boundary detection and phase separation, to the best of our knowledge, this current work represents the first study that demonstrates phase separation of PIV images based on the novel concepts of individual particle detection and Delaunay triangulation. This particle-based segmentation method offers several benefits compared to other existing approaches: (1) it is relatively insensitive to uneven illumination; (2) it outperforms intensity-based methods in virtually all test cases, especially when the tracer-particle seeding density is low; (3) it is able to determine interface locations with sub-pixel accuracy; and (4) it enables phase separation based on seeding density, a parameter relatively easy to control. This novel approach is expected to be useful in a broad range of applications and it certainly complements current methods that have been previously reported in the literature. Realistic representative experimental data is also presented to demonstrate the applicability of the method beyond synthetic images. The method is currently being applied in an automated fashion to a large PIV dataset concerning the dynamics of an unstable meniscus and associated velocity fields, which will be presented in a separate study that is underway.

Acknowledgments

This work was supported as a part of the Center for Geologic Storage of CO2, an Energy Frontier Research Center funded by the U.S. Department of Energy, Office of Science, BES, under award SC0C12504 (micromodel fabrication and a majority of experiments and analysis) and partially supported by the International Institute for Carbon-Neutral Energy Research (WPI-I2CNER), sponsored by the Japanese Ministry of Education, Culture, Sports, Science and Technology (part of experiments and analysis). Y. Li thanks the Faculty Excellence Grants and the Norm Asbjornson College of Engineering at Montana State University for their support.

References

[1] R. J. Adrian, Twenty years of particle image velocimetry, Experiments in Fluids 39 (2) (2005) 159–169.

[2] Y. Hassan, T. Blanchat, C. Seeley Jr, R. Canaan, Simultaneous velocity measurements of both components of a two-phase flow using particle image velocimetry, International Journal of Multiphase Flow 18 (3) (1992) 371–395.

[3] C. Brücker, Particle image velocimetry and associated techniques: PIV in two-phase flows, Von Karman Institute for Fluid Dynamics, Lecture Series 2000-01 (2000).

[4] D. Khalitov, E. K. Longmire, Simultaneous two-phase PIV by two-parameter phase discrimination, Experiments in Fluids 32 (2) (2002) 252–268.

[5] F. G. Ergin, B. B. Watz, N. F. Gade-Nielsen, A review of planar piv systems and image processing tools for lab-on-chip microfluidics, Sensors 18 (9) (2018) 3090.

[6] Y. Li, G. Blois, F. Kazemifar, K. T. Christensen, High-speed quantification of pore-scale multiphase flow of water and supercritical CO_2 in 2-d heterogeneous porous micromodels: flow regimes and interface dynamics, Water Resources Research 55 (5) (2019) 3758–3779.

[7] M. Simjoo, Y. Dong, A. Andrianov, M. Talanana, P. Zitha, CT scan study of immiscible foam

flow in porous media for enhancing oil recovery, Industrial & Engineering Chemistry Research 52 (18) (2013) 6221–6233.
[8] H. E. Dawson, P. V. Roberts, Influence of viscous, gravitational, and capillary forces on DNAPL saturation, Groundwater 35 (2) (1997) 261–269.
[9] A. Bazylak, Liquid water visualization in PEM fuel cells: A review, International Journal of Hydrogen Energy 34 (9) (2009) 3845–3857.
[10] H. E. Huppert, J. A. Neufeld, The fluid mechanics of carbon dioxide sequestration, Annual Review of Fluid Mechanics 46 (2014) 255–272.
[11] G. Blois, J. M. Barros, K. T. Christensen, A microscopic particle image velocimetry method for studying the dynamics of immiscible liquid–liquid interactions in a porous micromodel, Microfluid. Nanofluid. 18 (5-6) (2015) 1391–1406.
[12] F. Kazemifar, G. Blois, D. C. Kyritsis, K. T. Christensen, A methodology for velocity field measurement in multiphase high-pressure flow of CO_2 and water in micromodels, Water Resour. Res. 51 (4) (2015) 3017–3029.
[13] F. Kazemifar, G. Blois, D. C. Kyritsis, K. T. Christensen, Quantifying the flow dynamics of supercritical CO2–water displacement in a 2D porous micromodel using fluorescent microscopy and microscopic PIV, Advances in Water Resources 95 (2016) 352–368.
[14] Y. Li, F. Kazemifar, G. Blois, K. T. Christensen, Micro-PIV measurements of multiphase flow of water and liquid CO_2 in 2-D heterogeneous porous micromodels, Water Resour. Res. 53 (2017) 6178–6196.
[15] S. Roman, C. Soulaine, M. A. AlSaud, A. Kovscek, H. Tchelepi, Particle velocimetry analysis of immiscible two-phase flow in micromodels, Adv. Water Res. 95 (2016) 199–211.
[16] F. G. Ergin, Dynamic masking techniques for particle image velocimetry, Isı Bilimi ve Tekniği Dergisi 37 (2) (2017) 61–74.
[17] K. Kiger, C. Pan, PIV technique for the simultaneous measurement of dilute two-phase flows, J. Fluids Eng. 122 (4) (2000) 811–818.
[18] E. Delnoij, J. Westerweel, N. G. Deen, J. Kuipers, W. P. M. van Swaaij, Ensemble correlation PIV applied to bubble plumes rising in a bubble column, Chemical Engineering Science 54 (21) (1999) 5159–5171.
[19] Y. Niu, P. Mostaghimi, M. Shabaninejad, P. Swietojanski, R. T. Armstrong, Digital rock segmentation for petrophysical analysis with reduced user bias using convolutional neural networks, Water Resources Research 56 (2) (2020) e2019WR026597.
[20] B. Vennemann, T. Rösgen, A dynamic masking technique for particle image velocimetry using convolutional autoencoders, Experiments in Fluids 61 (7) (2020) 1–11.
[21] H. Liu, Y. Zhang, A. J. Valocchi, Lattice Boltzmann simulation of immiscible fluid displacement in porous media: Homogeneous versus heterogeneous pore network, Physics of Fluids 27 (5) (2015) 052103.
[22] C. Zhang, M. Oostrom, J. W. Grate, T. W. Wietsma, M. G. Warner, Liquid CO_2 displacement of water in a dual-permeability pore network micromodel, Environ. Sci. Technol. 45 (17) (2011) 7581–7588.
[23] L. Zuo, C. Zhang, R. W. Falta, S. M. Benson, Micromodel investigations of CO_2 exsolution from carbonated water in sedimentary rocks, Adv. Water Res. 53 (2013) 188–197.
[24] L. Gan, Detection of passive scalar interface directly from piv particle images in inhomogeneous turbulent flows, Flow, Turbulence and Combustion 97 (1) (2016) 141–170.
[25] S. Pfadler, F. Beyrau, A. Leipertz, Flame front detection and characterization using conditioned particle image velocimetry (cpiv), Optics Express 15 (23) (2007) 15444–15456.
[26] S. Schlüter, A. Sheppard, K. Brown, D. Wildenschild, Image processing of multiphase images obtained via x-ray microtomography: a review, Water Resources Research 50 (4) (2014) 3615–3639.
[27] W. Krause, X-ray contrast agents, in: Diagnostics of Vascular Diseases, Springer, 1997, pp. 99–113.
[28] D. Wildenschild, M. L. Rivers, M. L. Porter, G. C. Iltis, R. T. Armstrong, Y. Davit, Using synchrotron-based x-ray microtomography and functional contrast agents in environmental applications, Soil–water–root processes: Advances in tomography and imaging 61 (2013) 1–22.
[29] M. L. Porter, D. Wildenschild, G. Grant, J. I. Gerhard, Measurement and prediction of the relationship between capillary pressure, saturation, and interfacial area in a napl-water-glass bead system, Water Resources Research 46 (8) (2010).
[30] W. Kosiwczuk, A. Cessou, M. Trinite, B. Lecordier, Simultaneous velocity field measurements in two-phase flows for turbulent mixing of sprays by means of two-phase piv, Experiments in fluids 39 (5) (2005) 895–908.
[31] O. Carrier, F. G. Ergin, H.-Z. Li, B. B. Watz, D. Funfschilling, Time-resolved mixing and

flow-field measurements during droplet formation in a flow-focusing junction, Journal of Micromechanics and Microengineering 25 (8) (2015) 084014.

[32] X. Coron, J. Champion, M. Champion, Simultaneous measurements of velocity field and flame front contour in stagnating turbulent premixed flame by means of piv, in: Twelfth International Symposium on Applications of Laser Techniques to Fluid Mechanics, Citeseer, 2004.

[33] Y. Li, R. Grigoriev, M. Yoda, Experimental study of the effect of noncondensables on buoyancy-thermocapillary convection in a volatile low-viscosity silicone oil, Physics of Fluids 26 (12) (2014) 122112.

[34] Y. Li, M. Yoda, Convection driven by a horizontal temperature gradient in a confined aqueous surfactant solution: the effect of noncondensables, Experiments in fluids 55 (1) (2014) 1–11.

[35] Y. Li, M. Yoda, An experimental study of buoyancy-marangoni convection in confined and volatile binary fluids, International Journal of Heat and Mass Transfer 102 (2016) 369–380.

[36] A. Sanchis, A. Jensen, Dynamic masking of piv images using the radon transform in free surface flows, Experiments in fluids 51 (4) (2011) 871–880.

[37] K. Nakamura, H. J. Park, Y. Murai, T. Takeuchi, Thermal diffusion interface inside a horizontal pipe flow compared between laminar and turbulent flow regimes, Journal of Visualization 22 (4) (2019) 809–818.

[38] C. Jux, A. Sciacchitano, F. Scarano, Object surface reconstruction from flow tracers, Experiments in Fluids 62 (2) (2021) 1–19.

[39] E. M. Furst, Particle tracking with Matlab, University of Delaware, 2015.

[40] X. Song, F. Yamamoto, M. Iguchi, Y. Murai, A new tracking algorithm of piv and removal of spurious vectors using delaunay tessellation, Experiments in Fluids 26 (4) (1999) 371–380.

[41] F. Kazemifar, D. C. Kyritsis, Experimental investigation of near-critical CO_2 tube-flow and Joule–Thompson throttling for carbon capture and sequestration, Experimental Thermal and Fluid Science 53 (2014) 161–170.

[42] Y. Chen, Y. Li, A. J. Valocchi, K. T. Christensen, Lattice Boltzmann simulations of liquid CO_2 displacing water in a 2D heterogeneous micromodel at reservoir pressure conditions, Journal of Contaminant Hydrology 212 (2018) 14–27.

[43] A. Fakhari, Y. Li, D. Bolster, K. T. Christensen, A phase-field lattice Boltzmann model for simulating multiphase flows in porous media: Application and comparison to experiments of CO_2 sequestration at pore scale, Advances in Water Resources 114 (2018) 119–134.

[44] C. Chomsurin, C. J. Werth, Analysis of pore-scale nonaqueous phase liquid dissolution in etched silicon pore networks, Water Resour. Res. 39 (9) (2003).

[45] B. Zhao, C. W. MacMinn, R. Juanes, Wettability control on multiphase flow in patterned microfluidics, Proceedings of the National Academy of Sciences 113 (37) (2016) 10251–10256.

[46] W. B. Haines, Studies on the physical properties of soil. V. The hysteresis effect in capillary properties, and the modes of moisture distribution associated therewith, The Journal of Agricultural Science 20 (1) (1930) 97–116.